CrossMark
click for updates

Dysprosium electrodeposition from a hexaalkylguanidinium-based ionic liquid†

Claudia A. Berger,[a] Maria Arkhipova,[b] Gerhard Maas[b] and Timo Jacob*[a,c]

The rare-earth element dysprosium (Dy) is an important additive that increases the magnetocrystalline anisotropy of neodymium magnets and additionally prevents from demagnetizing at high temperatures. Therefore, it is one of the most important elements for high-tech industries and is mainly used in permanent magnetic applications, for example in electric vehicles, industrial motors and direct-drive wind turbines. In an effort to develop a more efficient electrochemical technique for depositing Dy on Nd-magnets in contrast to commonly used costly physical vapor deposition, we investigated the electrochemical behavior of dysprosium(III) trifluoromethanesulfonate in a custom-made guanidinium-based room-temperature ionic liquid (RTIL). We first examined the electrodeposition of Dy on an Au(111) model electrode. The investigation was carried out by means of cyclic voltammetry (CV) and X-ray photoelectron spectroscopy (XPS). The initial stages of metal deposition were followed by *in situ* scanning tunneling microscopy (STM). CV measurements revealed a large cathodic reduction peak, which corresponds to the growth of monoatomic high islands, based on STM images taken during the initial stages of deposition. XPS identified these deposited islands as dysprosium. A similar reduction peak was also observed on an Nd–Fe–B substrate, and positively identified as deposited Dy using XPS. Finally, we varied the concentration of the Dy precursor, electrolyte flow and temperature during Dy deposition and demonstrated that each of these parameters could be used to increase the thickness of the Dy deposit, suggesting that these parameters could be tuned simultaneously in a temperature-controlled flow cell to enhance the thickness of the Dy layer.

1. Introduction

The rare-earth element dysprosium (Dy) is rather unique amongst the magnetic materials, exhibiting both the highest magnetic moment per atom ($10\mu_B$) and the highest saturation magnetization of any element.[1] Therefore, it is no surprise that in its most prominent industrial application it is alloyed into neodymium–iron–boron magnets[2] in order to increase the magnetocrystalline anisotropy.[3] Neodymium–iron–boron magnets were invented by Sagawa *et al.* in 1984[4] and are now widely employed as magnetic field sources in hybrid electric vehicles and wind turbines,[5] for instance. Indeed, as early as 2007, 30 000 tons per year of neodymium magnets were being produced worldwide.[6] Current industrial methods rely on a combination of physical vapor deposition (PVD)[7] and sputtering techniques to produce Dy layers. The high energy cost of these methods, due to the high-vacuum conditions they require, makes them ecologically unsustainable, particularly at large scales. However, the electrochemical deposition of dysprosium from non-aqueous solvents has been put forward as a promising alternative to present industrial methods.[8] Room-temperature ionic liquids (RTILs) are organic salts, which are in the molten state at room-temperature.[9] Seemingly almost innumerable combinations of different anions and cations are possible, resulting in a vast variety of potential RTILs with tunable physicochemical properties that can be tailored for specific applications.[10] Besides well-investigated ionic liquids (ILs) with common imidazolium, pyridinium or piperidinium cations, there are new classes of ILs which are still being developed. One example here are RTILs, which already contain lanthanides in their anions and cations.[11–15] Another promising new class of ILs are hexaalkyl-substituted guanidinium salts, because of the flexibility that can be achieved by tuning each of the six alkyl groups independently.[16] In addition, they exhibit good thermal stability and are unreactive toward bases and most nucleophilic reagents due to the excellent charge stabilization in the peralkylated cation. Applications in electrochemistry have driven recent interest in RTILs, making their large electrochemical windows and high ionic conductivities

[a]*Institute of Electrochemistry, Ulm University, Albert-Einstein-Allee 47, 89081 Ulm, Germany. E-mail: Timo.Jacob@uni-ulm.de*
[b]*Institute of Organic Chemistry I, Ulm University, Ulm, Germany*
[c]*Helmholtz-Institute-Ulm (HIU), Ulm, Germany*

two of their most important features along with their low vapor pressures and high thermal stabilities.[17–22] Indeed, the fact that RTILs enable access to the electrodeposition of non-noble metals, which cannot be deposited from aqueous solutions, more than compensates for their high viscosities and costs, when considering their usefulness in a wide range of applications. One of these non-noble metals is dysprosium, the electrodeposition of which several groups have demonstrated from commercially available ionic liquids, e.g. phosphonium[23] or pyrrolidinium-based[8] RTILs. However, the deposition rates achieved in these studies were not yet sufficient, especially with a view to industrial applications. To address this need we investigated the electrodeposition of Dy from its triflate in a custom-made guanidinium-based ionic liquid. In the present work we characterize the electrodeposition of dysprosium first on Au(111) single crystal electrodes and then on Nd–Fe–B-magnets. Based on these results we discuss strategies for increasing the amount of deposited dysprosium on Nd–Fe–B magnets to achieve better permanent magnetic properties by variation of the concentration, flow of the electrolyte and temperature.

2. Experimental

Various guanidinium-based ionic liquids with the general composition $[C(NR_2^1)(NR_2^2)(NR_2^3)]^+A^-$ (R = alkyl, cycloalkyl; A^- = anion) were synthesized and examined with respect to their suitability for dysprosium deposition (see Table 1). Here, the two most significant factors were the width of the electrochemical potential window, especially in the cathodic potential region, and the amount of dissolved $Dy(OTf)_3$ without forming a precipitate in solution. Details of the synthesis and characterization of the applied guanidinium-based ILs can be found in the ESI† and in ref. 16, 24 and 25.

Based on the broad electrochemical potential window, a reasonable solubility of $Dy(OTf)_3$ and a relatively low viscosity of 108 mPa s (25 °C),[26] $N_{11}N_{11}N_{pip}GuaTFSI$ (pip = piperidin-1-yl) (see Fig. 1) was chosen as an appropriate electrolyte for dysprosium deposition. Additionally, a commercially available RTIL was used in the STM study, namely 1-butyl-3-methyl-imidazolium bis(trifluoromethylsulfonyl)imide (BMITFSI) (Merck KGaA, purity ≥ 99.5%, water ≤ 100 ppm, halides ≤ 100 ppm). The ionic liquids were vacuum-dried for 24 h at
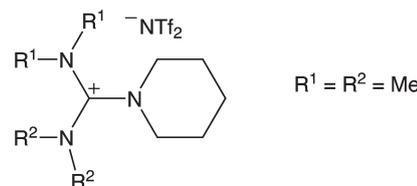

Fig. 1 Structure of the applied guanidinium-based ionic liquid, $[N_{11}N_{11}N_{pip}Gua]TFSI$.

elevated temperatures (80 °C, 2×10^{-4} mbar) before adding the precursor dysprosium triflate (98% $Dy(OTf)_3$, Sigma-Aldrich) to reach a concentration between 0.02 and 0.20 mol L^{-1} for the metal deposition.

CV and STM experiments, including handling and storage of the used substances, were performed inside a glove box under an argon atmosphere. During the transfer of the sample to the XPS chamber, air contact was inevitable due to the absence of an appropriate transfer vessel. Electrochemical investigations were carried out in self-designed cells made of KelF, each with a volume of 150 μl, and an Au(111) single crystal (MaTeck GmbH, Jülich, FRG) with a 12 mm diameter and Nd–Fe–B sintered square magnets with 10 mm edge lengths and 3 mm thickness (Vacuumschmelze GmbH & Co. KG, Hanau, Germany) acting as the working electrodes. Nd–Fe–B substrates were produced via sintering processes, resulting in rather rough surfaces. In this study, the calculated theoretical surface area was used for all charge determinations and current density evaluations, although the real surface area is supposedly larger. As counter and quasi-reference electrodes Pt wires (MaTeck GmbH, Jülich, FRG) were used; thus, all potentials are reported with respect to the Pt reference electrode. Prior to the measurements all electrodes (except Nd–Fe–B substrates) were annealed in a hydrogen flame and cooled down slowly in an argon stream.

All CVs were recorded with a Zahner IM6 potentiostat from Zahner Elektrik controlled by the Thales Z 1.20 USB software. Electrochemical in situ STM studies were performed with a Topometrix Discoverer TMX 2010. For the preparation of the STM tips, Pt/Ir wires (80 : 20) were electrochemically etched in 3.5 M NaCN and coated with BASF electrophoretic paint (ZQ84-3225) to reduce the faradaic current. All images were recorded in the constant-current mode with a tip current between 1–3 nA.

Table 1 Overview of features of synthesized guanidinium-based ionic liquids

Ionic liquid[a]	Cathodic limit vs. Pt/mV	Anodic limit vs. Pt/mV	Solubility $Dy(OTf)_3$/mol L^{-1}
$[N_{11}N_{22}N_{44}Gua]TFSI$	−1700	1000	>0.007
$[N_{11}N_{11}N_{44}Gua]OTf$	−800	1400	<0.026
$[N_{22}N_{44}N_{66}Gua]BF_4$	−1900	1300	>0.025
$[N_{11}N_{11}N_{pip}Gua]TFSI$	−2500	1500	<0.017
$[N_{11}N_{pip}N_{pip}Gua]TFSI$	−1800	1700	<0.200

[a] See the ESI for structural formulae.

The elemental composition of the sample surfaces was determined by X-ray photoelectron spectroscopy (XPS) measurements using monochromatized Al K_α (1486.6 eV) radiation (PHI 5800 MultiTechnique ESCA System, Physical Electronics). A surface spot of 0.8×0.8 mm^2 was used for all analyses. The measurements were performed with a detection angle of 45°, using pass energies at the analyzer of 93.9 and 29.35 eV for survey and detailed spectra, respectively. To calibrate the binding energies the C(1s) peak was set to 284.8 eV.

3. Results and discussion

3.1 Dy(OTf)$_3$/N$_{11}$N$_{11}$N$_{pip}$GuaTFSI on Au(111)

3.1.1 Cyclic voltammetry.
Fig. 2 shows the cyclic voltammograms of pure N$_{11}$N$_{11}$N$_{pip}$GuaTFSI (dashed line) and with addition of 0.02 mol L^{-1} Dy(OTf)$_3$ (solid line) on Au(111) recorded with a scan rate of 50 mV s^{-1}. The CV of the pure ionic liquid N$_{11}$N$_{11}$N$_{pip}$GuaTFSI shows a broad double-layer-type behavior over a potential range of about 3 V with a few small humps due to surface-related processes or minor impurities. The potential where the irreversible decomposition of the electrolyte takes place lies outside this potential range and remarkably occurs at low current densities around the reversal potentials in the CV. After adding 0.02 mol L^{-1} of Dy(OTf)$_3$, one can observe a single broad cathodic hump C_1 at -1 V vs. Pt, which indicates a possible reduction of dysprosium. We assume that Dy reduction proceeds in a single multi-electron transfer step from Dy(III) to Dy(0), as firstly no other cathodic processes could be observed, and secondly this behavior is reported in the literature for Dy deposition from other types of RTILs.[1,8,23] The reduction peak corresponds to a charge of 400 μC cm^{-2} as derived from the CV (Fig. 2). The charge complies with approximately 8×10^{14} Dy atoms, indicating slightly less than one monolayer of deposited Dy at this scan rate.

In the positive potential region we observe a large anodic peak, whose related charge is comparable to the cathodic peak. Based on the CV measurements alone, one cannot clearly distinguish whether this peak is caused by oxidation of Dy or decomposition of the ionic liquid. However, previous studies in other types of RTILs[1,8] claim the deposition of dysprosium to be an irreversible process, so we assume that the anodic process indicates more likely the oxidation of the ionic liquid. The comparison with the CV of the pure RTIL confirms this assumption, due to the increase of the current density at the positive reversal potential, which indicates the oxidation of the electrolyte.

3.1.2 In situ scanning tunneling microscopy.
For a more detailed characterization of the Dy deposition, in situ scanning tunneling microscopy (STM) measurements were performed. The obtained STM images are shown in Fig. 3. Fig. 3(a) shows the bare Au surface with several step edges at positive potentials, i.e. 300 mV vs. Pt. Fig. 3(b) is recorded at very negative potentials (-1.6 V vs. Pt), which means potentials in the region of the reduction peak in the CV (see Fig. 2). Here, the beginning of the growth of monoatomic high islands on the Au terraces can be observed, which could indicate Dy deposition. Unfortunately, we were not able to record further STM images of the deposition process in this system. We suppose that the guanidinium cations form a dense and disordered adsorbate structure at very negative potentials, which compromises the STM measurement by blurring of the STM images. Therefore, the STM investigation of this system is a formidable task. However, investigations in an alternative RTIL, namely 1-butyl-3-methylimidazolium bis(trifluoromethylsulfonyl)imide (BMITFSI), showed more details of the dysprosium deposition (Fig. 4).
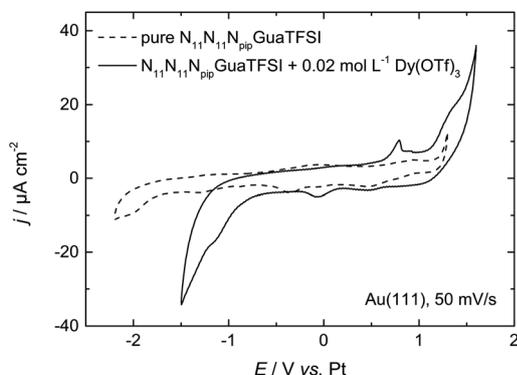

Fig. 3 In situ STM images of Dy(OTf)$_3$/N$_{11}$N$_{11}$N$_{pip}$GuaTFSI on Au(111) at (a) 300 mV and (b) −1600 mV.

Fig. 4 In situ STM images of Dy(OTf)$_3$/BMITFSI on Au(111) at (a) −200 mV and (b) −800 mV.

Fig. 2 CV of N$_{11}$N$_{11}$N$_{pip}$GuaTFSI (dashed line) and N$_{11}$N$_{11}$N$_{pip}$GuaTFSI + 0.02 mol L^{-1} Dy(OTf)$_3$ (solid line) on Au(111) at a scan rate of 50 mV s^{-1}.
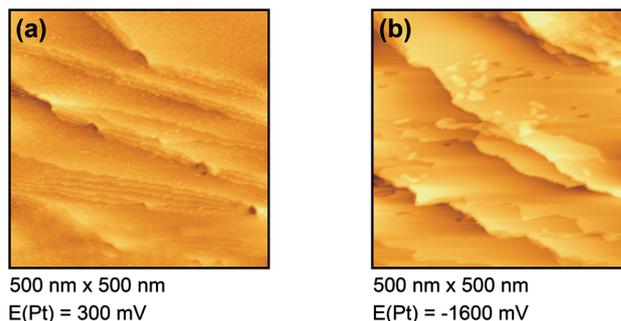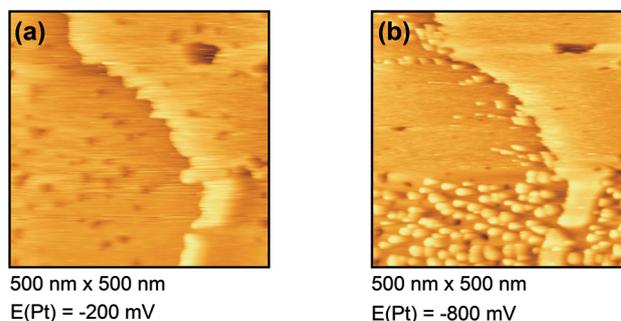
Fig. 4(a) shows the free Au surface at relatively positive potentials (−200 mV *vs.* Pt), comparable to Dy(OTf)$_3$ in N$_{11}$N$_{11}$N$_{pip}$GuaTFSI. After decreasing the potential the formation of islands can be observed (see Fig. 4(b)). The formation of the islands seems to start at step edges and then to spread over the Au terraces. The derived height of the islands from this STM image is approximately 300 nm.

3.1.3 X-ray photoelectron spectroscopy. Further insight into the chemical composition of the sample was gained by XPS measurements. Fig. 5 shows the detailed XP survey spectra of Dy(4d) and O(1s) signals obtained directly following the electrodeposition of Dy from Dy(OTf)$_3$/N$_{11}$N$_{11}$N$_{pip}$GuaTFSI on Au(111). As mentioned before, we expect to detect dysprosium in the form of Dy$_2$O$_3$ due to the inevitable air contact during transportation to the XPS device. In the detailed spectrum, the Dy(4d) peak shows a more complex shape than expected from sole spin–orbit splitting, which has been reported in the literature and is attributed to final state multiplet coupling between the 4d and 4f states.[27] Here, the peak with the highest intensity is centered at a binding energy of 157.0 eV and it possesses an additional shoulder of lower intensity around 154.9 eV. The binding energy of the absolute maximum is in relatively good agreement with binding energies for Dy$_2$O$_3$ reported in the literature.[28,29] Further, the detailed spectrum for O(1s) is shown in Fig. 5. Here, the O(1s) peak is observable at a binding energy of 532.0 eV. Comparable values have been reported in the literature[28,29] and were assigned to the adsorbed OH-groups and (bi)carbonates on the Dy$_2$O$_3$ deposit due to the reactivity of lanthanides toward air and moisture.
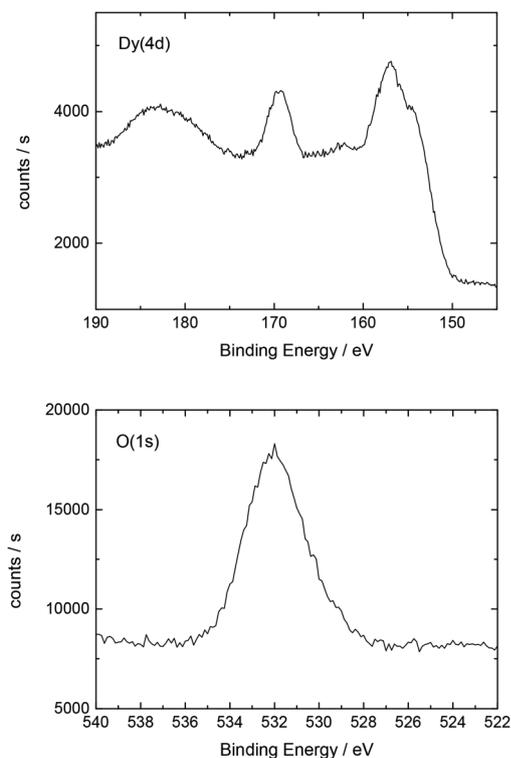

Fig. 5 Detailed XP spectrum of the Dy deposit on Au(111).

Table 2 Atomic concentration of Dy on Au(111)

O(1s)	C(1s)	F(1s)	Dy(4d)	S(2p)	Au(4f)
51.0	16.3	15.7	10.6	5.0	1.4

Additionally, Table 2 shows the determined atomic concentrations on the sample surface after electrochemical Dy deposition on Au(111). Here, the ratio of O/Dy is around 5, which is much higher than the expected value for stoichiometric Dy$_2$O$_3$. This observation has also been reported in the literature[29] and could be due to the presence of excess oxygen on the surface of the deposited films, as mentioned before.

3.2 Dy(OTf)$_3$/N$_{11}$N$_{11}$N$_{pip}$GuaTFSI on NdFeB

3.2.1 Cyclic voltammetry. Fig. 6 shows the first cycles of the cyclic voltammograms of N$_{11}$N$_{11}$N$_{pip}$GuaTFSI containing 0.063 mol L^{-1} of Dy(OTf)$_3$ (black curve) and 0.200 mol L^{-1} of Dy(OTf)$_3$ (red curve) on a Nd–Fe–B magnet recorded with a scan rate of 10 mV s^{-1}. After adding 0.063 mol L^{-1} of Dy(OTf)$_3$ to the RTIL, one can observe a single broad cathodic hump, C$_1$, at around −1.2 V *vs.* Pt, which also indicates a possible deposition of dysprosium. According to literature, the electrodeposition is supposed to proceed from Dy(III) to Dy(0) in a single one-step electron transfer.[1,8,23] This reduction peak corresponds to a charge of 60 mC cm^{-2} during the deposition process as derived from the CV (Fig. 6), which complies with 10^{17} Dy atoms per cm^2 (geometrically calculated area). Here, no clear oxidation peak was detected, but a slight increase in the current density at potentials >0.2 V can be observed, which could be an indication of a partial dissolution of Dy.

As the first attempt to increase the amount of deposited dysprosium, and thereby improve the permanent magnetic properties of the material, the concentration of the dissolved Dy salt in the RTIL was increased by a factor of 3. The red curve in Fig. 6 shows the CV of 0.200 mol L^{-1} of Dy(OTf)$_3$/N$_{11}$N$_{11}$N$_{pip}$GuaTFSI on Nd–Fe–B. Here, one can clearly notice an increase of the charge flow during the deposition process and dissolution, respectively. This also confirms the assumption of Dy oxidation at positive potentials of 0.2 V. The charge
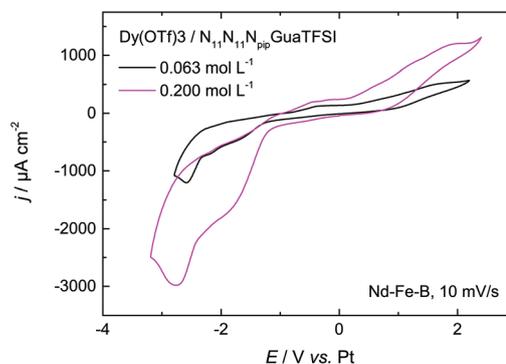

Fig. 6 CV of 0.063 mol L^{-1} and 0.200 mol L^{-1} of Dy(OTf)$_3$ + N$_{11}$N$_{11}$N$_{pip}$GuaTFSI on Nd−Fe−B, recorded with a scan rate of 10 mV s^{-1}.

associated with the cathodic processes was enhanced from 60 mC cm^{-2} (Fig. 6, black curve) to 150 mC cm^{-2} (Fig. 6, red curve) over the same potential range, *i.e.* the charge and thus the amount of deposited Dy atoms (3×10^{17} per cm^2) are almost tripled.

3.2.2 X-ray photoelectron spectroscopy. Here, also XPS measurements were performed in order to identify the obtained deposit. Fig. 7 shows the detailed XP survey spectra of Dy(4d) and O(1s) obtained directly after electrodeposition of Dy from Dy(OTf)$_3$/N$_{11}$N$_{11}$N$_{pip}$GuaTFSI on Nd–Fe–B. Analogous to section 3.1.3, we expect to detect dysprosium in the form of Dy$_2$O$_3$ due to the inevitable air contact during transportation to the XPS chamber. In the detailed spectrum, the Dy(4d) peak shows also the complex shape, which was observed in Fig. 5. The main peak appears at a binding energy of 157.0 eV, which very likely indicates Dy in the form of Dy$_2$O$_3$, according to the literature.[28,29] Further, the detailed spectrum for O(1s) is shown in Fig. 7. Here, the O(1s) peak is observable at a binding energy of 531.5 eV, which is also in good agreement with the literature and is an indication for (bi)carbonates and OH-groups adsorbed on the surface.[28,29]

Additionally, Table 3 shows the determined atomic concentrations on the sample surface after electrodeposition of Dy on Nd–Fe–B. Here, the ratio of O/Dy is around 2.5, which is again higher than the expected value for stoichiometric Dy$_2$O$_3$. We assume that this observation could be due to the presence of excess oxygen in the form of adsorbed OH-groups or carbo-

Table 3 Relative atomic concentration of Dy on Nd–Fe–B

C(1s)	O(1s)	Dy(4d)	F(1s)	Fe(2p)	Nd(4d)
47.2	32.3	12.6	6.3	1.1	0.5

nates on the surface of the deposited films or at least partial oxidation of the various components of the substrate.

3.3 Increasing Dy layer thickness on Nd–Fe–B

3.3.1 Flow cell. After the basic electrochemical characterization, the influence of a flow cell on dysprosium deposition from Dy(OTf)$_3$/N$_{11}$N$_{11}$N$_{pip}$GuaTFSI on Nd–Fe–B was investigated. For this purpose, a potential of 2 V *vs.* Pt was applied to the system, *i.e.* the potential region of Dy deposition, and the resulting current was recorded over time. Here, all single measurements were performed at room temperature. Fig. 8 shows *I–t* transients for flow rates of the electrolyte of 0 ml h^{-1} (grey curve), 3 ml h^{-1} (black curve) and 4 ml h^{-1} (red curve). It has to be mentioned that the aberration in the red curve is caused by a brief disruption of the electrolyte flow. The charges related to Dy reduction were determined by integration of the particular transient over the first 800 seconds. For no electrolyte flow (0 ml h^{-1}), we determined a charge of 2.3 mC cm^{-2} for Dy deposition. For a flow rate of 3 ml h^{-1}, the derived charge amounts to 38.5 mC cm^{-2}, which signifies a massive increase. Finally, a 4 ml h^{-1} flow rate leads to a maximum charge of 122.5 mC cm^{-2}, which means about 2.5×10^{17} Dy atoms per cm^2 of the Nd–Fe–B substrate. According to our experience implementation of even higher flow rates of the electrolyte is not manageable due to the generally high viscosity of ILs.

3.3.2 Temperature-controlled cell. Fig. 9 shows *I–t* transients recorded over 4 hours for the system Dy(OTf)$_3$/N$_{11}$N$_{11}$N$_{pip}$GuaTFSI on Nd–Fe–B. The *I vs. t* measurements were performed analogous to section 3.3.1. The sole difference is the absence of electrolyte flow, which means constant electrolyte volume, and the differing temperatures of the single experiments. The overall charge flow due to dysprosium
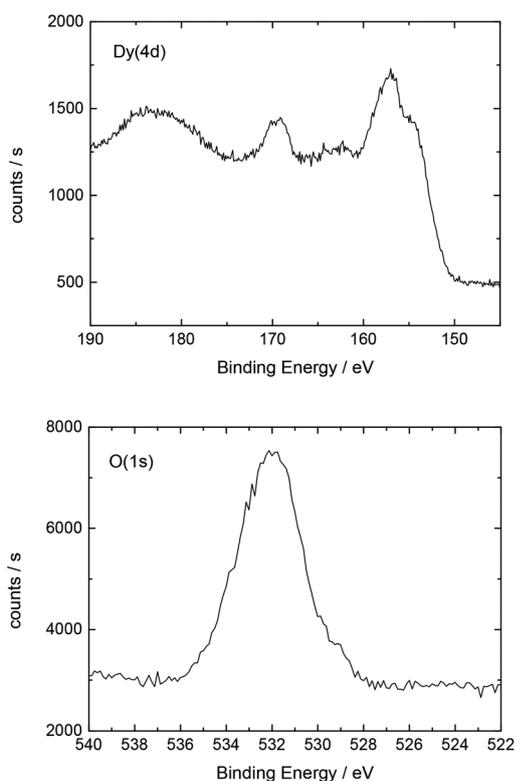

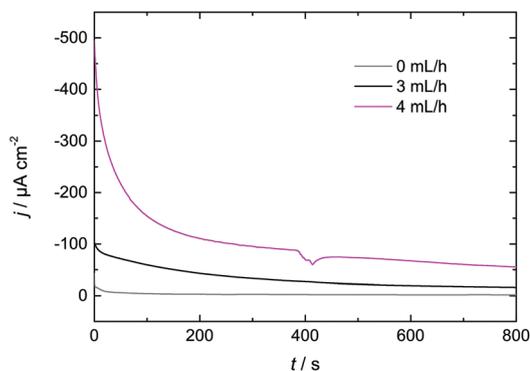**Fig. 7** Detailed XP spectrum of the Dy deposit on the Nd–Fe–B magnet.

Fig. 8 Flow rate dependence of *I–t*-transients during Dy deposition from Dy(OTf)$_3$/N$_{11}$N$_{11}$N$_{pip}$GuaTFSI on Nd–Fe–B.
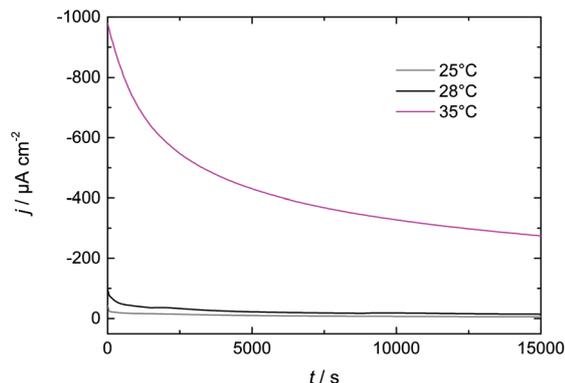
Fig. 9 Temperature dependence of I–t-transients during Dy deposition from Dy(OTf)$_3$/N$_{11}$N$_{11}$N$_{pip}$GuaTFSI on Nd–Fe–B.

reduction was determined for the first 30 minutes by integration of the I–t transients for 25 °C (grey curve), 28 °C (black curve) and 35 °C (red curve). While we obtain 32.0 mC cm^{-2} for 25 °C, increasing the temperature by only three degrees to 28 °C results in an increased charge of 69.8 mC cm^{-2}. A further increase of the temperature up to 35 °C results in a maximum charge of 192.4 mC cm^{-2}, translating to an overall deposition coverage of 145 × 10^{16} dysprosium atoms per cm^2 of the Nd–Fe–B substrate.

4. Conclusions

In this paper we have investigated Dy electrodeposition from a tailored guanidinium-based RTIL on Au(111) as well as Nd–Fe–B substrates. In the presence of Au(111) we found that the reduction of Dy(III) to Dy(0) occurs in a single step at <−1 V vs. Pt. The reduction of Dy coincides with the formation of monoatomic high islands on the Au terraces which were observed in *in situ* STM and positively identified as Dy deposits on the Au(111) electrode surface in XPS measurements.

A single reduction step at <−1 V vs. Pt was also observed in the presence of the Nd–Fe–B substrate, which is comparable to the behavior obtained for Au(111). The XP spectra confirmed the presence of Dy on the magnet's surface. We were able to enhance the thickness of the deposited Dy layer by either increasing the electrolyte flow or increasing the temperature. Thus, we expect that a combination of both approaches could be used to further optimize the thickness of the deposited Dy for industrial applications. This optimization could be realized *via* a temperature-controlled flow cell, resulting in improvements in the magnetic properties of the Nd–Fe–B substrate at a reduced energetic cost.

Acknowledgements

References

1 J. Lodermeyer, M. Multerer, M. Zistler, S. Jordan, H. J. Gores, W. Kipferl, E. Diaconu, M. Sperl and G. Bayreuther, *J. Electrochem. Soc.*, 2006, **153**, C242–C248.

2 N. Oono, M. Sagawa, R. Kasada, H. Matsui and A. Kimura, *J. Magn. Magn. Mater.*, 2011, **323**, 297–300.

3 M. Sagawa, S. Fujimura, H. Yamamoto, Y. Matsuura and K. Hiraga, *IEEE Trans. Magn.*, 1984, **MAG-20**, 1584.

4 M. Sagawa, S. Fujimura, N. Togawa, H. Yamamoto and Y. Matsuura, *J. Appl. Phys.*, 1984, **55**, 2083–2087.

5 S. Hoenderdaal, L. T. Espinoza, F. Marscheider-Weidemann and W. Graus, *Energy*, 2013, **49**, 344–355.

6 K. Miura, M. Itoh and K.-I. Machida, *J. Alloys Compd.*, 2008, **466**, 228–232.

7 H. Sepehri-Amin, T. Ohkubo and K. Hono, *J. Appl. Phys.*, 2010, **107**, 09A745.

8 G. Suppan, M. Ruehrig, A. Kanitz and H. J. Gores, *J. Electrochem. Soc.*, 2015, **162**, D382–D388.

9 K. R. Seddon, *J. Chem. Technol. Biotechnol.*, 1997, **68**, 351–356.

10 H. Tokuda, K. Hayamizu, K. Ishii, M. A. Bin Hasan Susan and M. Watanabe, *J. Phys. Chem. B*, 2005, **109**, 6103–6110.

11 P. Nockemann, B. Thijs, N. Postelmans, K. V. Hecke, L. V. Meervelt and K. Binnemans, *J. Am. Chem. Soc.*, 2006, **128**, 13658–13659.

12 P. Nockemann, B. Thijs, S. Pittois, J. Thoen, C. Glorieux, K. V. Hecke, L. V. Meervelt, B. Kirchner and K. Binnemans, *J. Phys. Chem. B*, 2006, **110**, 20978–20992.

13 B. Mallick, B. Balke, C. Felser and A.-V. Mudring, *Angew. Chem., Int. Ed.*, 2008, **47**, 7635–7638.

14 D. Prodius, F. Macaev, Y. Lan, G. Novitchi, S. Pogrebnoi, E. Stingaci, V. Mereacre, C. E. Anson and A. K. Powell, *Chem. Commun.*, 2013, **49**, 9215–9217.

15 C. Lu, S. Das, N. Siraj, P. K. S. Magut, M. Li and I. M. Warner, *J. Phys. Chem. A*, 2015, **119**, 4780–4786.

16 H. Kunkel and G. Maas, *Eur. J. Org. Chem.*, 2007, 3746–3757.

17 F. Endres, *ChemPhysChem*, 2002, **3**, 144–154.

18 R. D. Rogers and K. R. Seddon, *Science*, 2003, **302**, 792–793.

19 M. J. Earle, J. M. S. S. Esperanca, M. A. Gilea, J. N. Canongia Lopes, L. P. N. Rebelo, J. W. Magee, K. R. Seddon and J. A. Widegren, *Nature*, 2006, **439**, 831–834.

20 F. Endres and S. Zein El Abedin, *Phys. Chem. Chem. Phys.*, 2006, **8**, 2101–2116.

21 F. Endres, D. MacFarlane and A. Abbott, *Electrodeposition from Ionic Liquids*, Wiley-VCH, Weinheim, 2008.

22 M. Freemantle, *An Introduction to Ionic Liquids*, Royal Society of Chemistry, Cambridge, 2009.

23 A. Kurachi, M. Matsumiya, K. Tsunashima and S. Kodama, *J. Appl. Electrochem.*, 2012, **42**, 961–968.

24 W. Kantlehner, E. Haug, W. W. Mergen, P. Speh, T. Maier, J. J. Kapassakalidis, H.-J. Bräuner and H. Hagen, *Liebigs Ann. Chem.*, 1984, **1984**, 108–126.

25 M. Gnahm, C. Berger, M. Arkhipova, H. Kunkel, T. Pajkossy, G. Maas and D. M. Kolb, *Phys. Chem. Chem. Phys.*, 2012, **14**, 10647–10652.

26 N. Bucher, S. Hartung, M. Arkhipova, D. Yu, P. Kratzer, G. Maas, M. Srinivasan and H. E. Hoster, *RSC Adv.*, 2014, **4**, 1996–2003.

27 H. Ogasawara, A. Kotani and B. T. Thole, *Phys. Rev. B: Condens. Matter Mater. Phys.*, 1994, **50**, 12332.

28 D. Barreca, A. Gasparotto, A. Milanov, E. Tondello, A. Devi and R. A. Fischer, *Surf. Sci. Spectra*, 2007, **14**, 52–59.

29 A. P. Milanov, T. Toader, H. Parala, D. Barreca, A. Gasparotto, C. Bock, H.-W. Becker, D. K. Ngwashi, R. Cross, S. Paul, *et al.*, *Chem. Mater.*, 2009, **21**, 5443–5455.